SKA-low intensity mapping pathfinder updates: deeper 21 cm power spectrum limits from improved analysis frameworks

Nichole Barry[a,b] **Gianni Bernardi**[c,d,e] **Bradley Greig**[a,b] **Nicholas Kern**[f,*] **and Florent Mertens**[g,h]

[a]University of Melbourne, School of Physics, Parkville, VIC, Australia
[b]ARC Centre of Excellence for All Sky Astrophysics in 3 Dimensions (ASTRO-3D)
[c]INAF – Istituto di Radioastronomia, Bologna, Italy
[d]Rhodes University, Department of Physics and Electronics, Grahamstown, South Africa
[e]South African Radio Astronomy Observatory, Black River Park, Observatory, Cape Town, South Africa
[f]Massachusetts Institute of Technology, Department of Physics and Kavli Institute for Astrophysics and Space Research, Cambridge, Massachusetts, United States
[g]PSL Research University, CNRS, Sorbonne Université, LERMA, Observatoire de Paris, Paris, France
[h]University of Groningen, Kapteyn Astronomical Institute, AV Groningen, The Netherlands

Abstract. The Square Kilometer Array (SKA) is a planned radio interferometer of unprecedented scale that will revolutionize low-frequency radio astronomy when completed. In particular, one of its core science drivers is the systematic mapping of the Cosmic Dawn and Epoch of Reionization, which mark the birth of the first stars and galaxies in the universe and their subsequent ionization of primordial intergalactic hydrogen, respectively. The SKA will offer the most sensitive view of these poorly understood epochs using the redshifted 21-cm hyperfine signal from intergalactic hydrogen. However, significant technical challenges stand in the way of realizing this scientific promise. These mainly involve the mitigation of systematics coming from astrophysical foregrounds, terrestrial radio interference, and the instrumental response. The Low Frequency Array, the Murchison Widefield Array, and the Hydrogen Epoch of Reionization Array are SKA pathfinder experiments that have developed a variety of strategies for addressing these challenges, each with unique characteristics that stem largely from their different instrumental designs. We outline these various directions, highlighting key differences and synergies, and discuss how these relate to the future of low-frequency intensity mapping with the SKA. We also briefly summarize the challenges associated with modeling the 21-cm signal and discuss the methodologies being proposed for inferring constraints on astrophysical models. [DOI: 10.1117/1.JATIS.8.1.011007]

Keywords: astronomy; interferometry; telescopes.

Paper 21091SS received Aug. 13, 2021; accepted for publication Oct. 21, 2021; published online Nov. 18, 2021.

1 Introduction

Low-frequency radio observations ($50 < \nu < 200$ MHz) of the redshifted 21 cm line from neutral hydrogen are some of the most promising probes of the Epoch of Reionization (EoR) and the era marking the birth of the first luminous structures in the universe, known as Cosmic Dawn (CD).[1–4] The aim of these radio observations, known as intensity mapping surveys, is to scan the sky to produce maps of 21 cm emission and to use their large frequency bandwidths as a tool to probe the evolution of the 21-cm signal across redshift. These measurements would transform our understanding of the properties of the first stars and galaxies and shed light on the evolution

*Address all correspondence to Nicholas Kern, nkern@mit.edu

2329-4124/2021/$28.00 © 2021 SPIE

of primordial gas in the intergalactic medium (IGM). In addition, 21-cm observations of the EoR and CD can be used in conjunction with other cosmological probes to help pin down constraints on ΛCDM cosmology.[5]

However, a key technical challenge plagues these efforts; contaminating galactic and extragalactic foreground emission is orders of magnitude brighter than the underlying cosmological signal of interest. This sets up a delicate signal separation problem, which is compounded by the fact that neither the 21-cm cosmological signal, the low-frequency foreground sky, nor the instrumental response of the telescope are known *a priori* by the observer to high precision. This forms the basis of the 21-cm foreground separation problem. Although the early view of the problem was to model the spatial and spectral properties of the foregrounds to subtract them (e.g., Refs. 6–9), the last decade has seen a shift toward an "avoidance versus subtraction" paradigm: the former approach assumes foregrounds cannot be modeled and simply discards contaminated data, whereas the latter attempts to carefully clean the data of contamination through precise sky modeling.

Foreground emission is generally smooth as a function of frequency owing to its largely nonthermal origin, whereas the 21-cm signal is highly spectrally variant, as it probes the inhomogeneities of the IGM along the observer's line-of-sight. Because of this, foregrounds occupy a well-defined, wedge-like region in the transverse and line-of-sight Fourier domains ($k_\perp$–$k_\parallel$, respectively; $k_\perp$ is proportional to baseline length and $k_\parallel$ is proportional to the Fourier conjugate of frequency),[10] leaving an uncontaminated region where the high-redshift 21-cm signal is theoretically free of contaminants (the "EoR window"; Refs. 11–14). This ideal scenario is, in practice, degraded by any instrumental response that corrupts the smooth-spectrum foregrounds, eventually leaking its power into the otherwise pristine EoR window. The foreground separation problem then turns into a joint foreground characterization and instrument calibration problem, i.e., how to best correct the instrumental response and simultaneously preserve the foreground spectral smoothness while modeling and improving our understanding of the low-frequency sky.

As the next generation of EoR and CD intensity mapping telescopes are designed and built, including the Square Kilometer Array (SKA), it is useful to review some of the recent advances made in experimental design and data analysis. In particular, this paper summarizes recent progress made by three SKA pathfinder radio interferometers (Fig. 1): the Murchison Widefield Array (MWA), the Low Frequency Array (LOFAR), and the Hydrogen Epoch of Reionization Array (HERA). We highlight their distinct approaches to data analysis informed by their instrumental design, as well as some of their synergistic properties. We detail their design specifications in Table 1, including the planned design of SKA-Low, highlighting its order-of-magnitude increase in collecting area relative to the current pathfinder experiments. Much of their shared technical challenges revolve around the fundamental systematics facing 21-cm interferometric experiments. Note that the interferometric telescopes discussed in this paper are distinct from

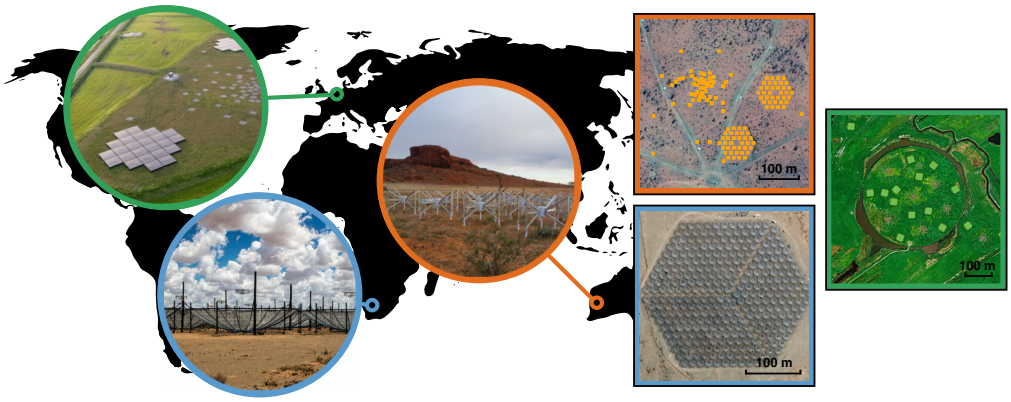

Fig. 1 The three SKA-low intensity mapping pathfinder experiments, including (from left to right) LOFAR, HERA, and the MWA (Phase II EoR layout). We show the array layouts of the experiments (right insets), demonstrating the differences in their antenna array layout. Satellite image credit: Google and Maxar Technologies.

Table 1 SKA pathfinder experiment specifications.

Parameter	MWA[a]	LOFAR[15]	HERA[16]	SKA–Low[b]
Latitude, longitude (deg)	−26.7, 116.6	52.9, 6.9	−30.7, 21.4	−26.8, 116.8
Element size (m)	5	30.75	14	38
Number of elements	128	76	350	512
Collecting area (m^2)	$\mathcal{O}(10^3)$	$\mathcal{O}(10^4)$	$\mathcal{O}(10^4)$	$\mathcal{O}(10^5)$
Min. baseline length (m)	7.7 (7.1)	68	14.6	40
Max. baseline length (m)	2873 (687)	2×10^6	876	65000
Angular resolution[c] (arcmin)	2 (6)	3×10^{-3}	11	0.15
Field of view[c] (FWHM) (deg)	25	3.8	9	3
Frequency coverage (MHz)	80 to 300	30 to 190	50 to 230	50 to 350

[a]Phase I (Phase II) MWA EoR layout.
[b]Planned design as of Ref. 17.
[c]Angular resolution and field of view quoted at 150 MHz.

21-cm experiments targeting the "global signal" or the monopole signal (e.g., Ref. 18), although they share many similar technical challenges. Largely, these challenges distill down to celestial, terrestrial, and instrumental systematics that impede the observers' ability to separate foreground signals from 21 cm signals, which we summarize below.

1.1 *Incomplete Sky Models*

Instrument calibration assumes that the sky model is known and perfectly represented. However, sky models are generally made from a catalog of point sources, derived from previous observations with a given sensitivity and angular resolution, which is inevitably incomplete. Missing sources in the calibration model lead to spurious emission, often below the noise level,[19] that corrupts the foreground spectral smoothness, contaminating the EoR window.[1,20] Moreover, radio sources exhibit a rich morphology, with jets and lobes that often extend over a range of angular scales: observations that fail to sample the full morphology inevitably lead to a calibration bias that, again, leaks foreground power into the EoR window.[21]

1.2 *Primary Beams*

Unlike steerable dish antennas, dipole arrays are mostly constituted of dipole clusters that are digitally pointed to a sky direction, resulting in primary beams that vary with time, which can be nontrivial to model. In addition, primary beams have an intrinsic frequency dependence, particularly in the sidelobe region. Unmodeled variability in the primary beam sidelobes will inevitably corrupt off-axis foreground spectral smoothness and therefore leak into the EoR window (e.g., Refs. 22–25). Moreover, mutual coupling tends to complicate the spatial and spectral beam structure, exacerbating beam-to-beam differences (e.g., Ref. 26). Measuring, modeling, and mitigating primary beams effects are at the forefront of active research,[27–29] as they introduce biases that are difficult to correct for both standard and redundant calibration approaches.

1.3 *Ionosphere*

The partially ionized layer located between ∼50 and 1000 km above the surface of the Earth interacts with the celestial signal at low frequencies. Absorption, scattering, and defocusing of the incoming wavefronts are due to temporal and spatial variations of the ionospheric electron density content, leading to a sky position and time-dependent point spread function. Ionospheric

effects are routinely mitigated by building up a sky model and subsequently calibrating each sky source independently. This approach produces virtually artifact-free images,[30,31] at the cost of extracomputation. Theoretically, small offsets that lead to imperfect ionospheric calibration may lead to negligible contamination to short baselines.[32] Fortunately, evidence suggests that most data are not severely affected by ionospheric effects at EoR frequencies.[33] However, the accidental inclusion of ionospherically active data can obscure the 21 cm signal.[34] Ionospheric effects are dependent on λ^2, and thus CD analyses are more affected and must perform more mitigation.[35]

1.4 *Baseline Dependent Effects*

Some effects cannot be factored and modeled by antenna-based terms and, therefore, cannot be treated on a per-antenna basis. Two examples of such errors are cross-coupling and radio frequency interference (RFI). Cross-coupling can group together a number of instrumental effects ranging from primary beams affected by mutual coupling and actual cross-talk along the radio frequency system.[26,36] Mitigation of some of these effects can be done in hardware,[37] whereas others can be carried out in a semiempirical fashion (e.g., Ref. 38), as detailed physical modeling requires an extremely accurate knowledge of the whole signal chain and is different for each instrument.

RFI is a well-known problem for radio observations and advanced methods have already been developed to deal specifically for low-frequency observations where the RFI environment is often more severe (e.g., Refs. 39–41). Very faint RFI that cannot be detected and excised directly in the visibility data may be a significant contaminant to the EoR signal and also lead to a calibration bias. Techniques to identify and remove data affected by faint RFI are actively being developed.[42]

Recent developments in addressing some of the aforementioned systematics, some at the hardware level others at the analysis level, have led to improved constraints on the upper limit of the 21-cm power spectrum at the EoR and CD, summarized in Fig. 2. We also plot fiducial power spectrum models, showing a few orders of magnitude in sensitivity still needed to make a

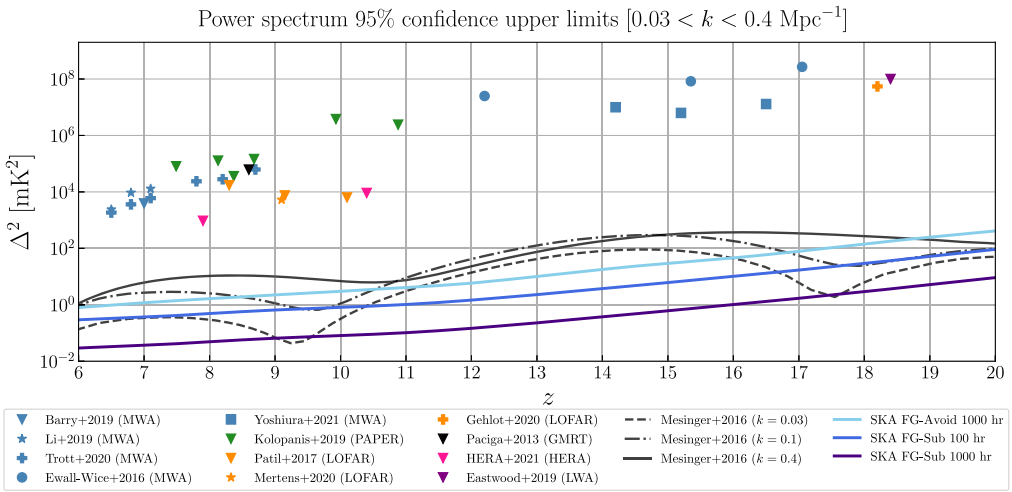

Fig. 2 Upper limits on the 21-cm power spectrum at 95% confidence (2σ) from various experiments from $6 < z < 20$ spanning a range of wavevectors, k. The redshift range is chosen to focus on recent limits from SKA pathfinders. The theoretical power spectrum from the faint galaxies EoR simulation of Ref. 43 is plotted as solid and dashed black lines. While 21-cm interferometric experiments have steadily pushed down in sensitivity over the past 5 years, fiducial models remain a couple orders of magnitude deeper. Projected 2σ sensitivity curves for the SKA assuming foreground avoidance at $k = 0.4$ Mpc^{-1} (FG-avoid) and foreground subtraction at $k = 0.1$ Mpc^{-1} (FG-Sub) are also plotted for a 100-h and 1000-h integration. The SKA-low sensitivity is computed using the latest available stations layout as of July 2021 and latest single station sensitivity estimates.[44]

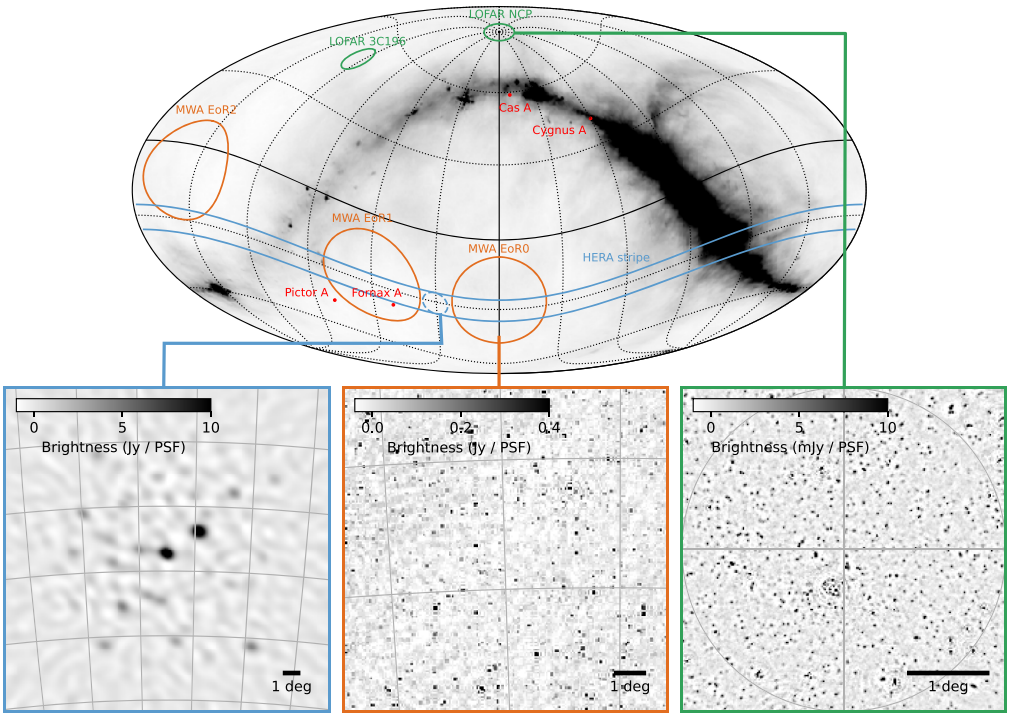

Fig. 3 Images of the fields observed by the three SKA pathfinder experiments. At the top, we show a map of the low-frequency galactic foregrounds,[45,46] highlighting the main observing fields of HERA (Phase I; blue), MWA (Phase I; orange), and LOFAR (green), as well as the locations of a few prominent radio sources (e.g., Fornax A). At the bottom, we show representative images taken by each of the experiments illustrating the distinctive fields of view and spatial resolutions (reproduced with permission from Refs. 36, 47, and 48).

fiducial detection. We also plot forecasted noise curves from the SKA under different time integration and foreground mitigation assumptions, showing it will be able to detect these models across a wide range of redshifts at high significance, assuming systematics can be mitigated. Figure 3 shows a map of the low-frequency sky, highlighting parts where the SKA pathfinders have set their most sensitive upper limits on the power spectrum, with representative images of those foregrounds with each of the experiments.

In the following sections, we review improved limits from the MWA, LOFAR, and HERA and discuss some of the developments that enabled these improvements. In addition, we discuss some of the challenges in theoretical simulation of the 21-cm signal and the interpretation of these upper limits for placing constraints on astrophysical models of the EoR and CD.

2 Murchison Widefield Array

The MWA[49–51] is a first-generation low-frequency radio interferometer located in the Murchison Shire of Western Australia. The MWA is an observatory; it has a wide-range of use-cases ranging from extragalactic studies of clusters and AGN, to nearby studies of our own galaxy and Sun. One of its main scientific objectives, however, is to measure the elusive 21 cm signal from our early universe and has been observing three low-foreground fields on the sky (EoR0, EoR1, and EoR2; see Fig. 1) in search of the EoR and CD since 2013.

To reduce the number of observations required to reach EoR sensitivities, ultrawide field-of-views are built into the design of the MWA. This is achieved through the use of beam-formed elements, consisting of a 4×4 grid of dual-polarization dipoles over a ground screen. The frequencies of interest for EoR observations with the MWA range from 139 to 197 MHz (e.g., Ref. 25), which probes $z = 9.3 - 6.2$, but earlier epochs can be observed up to $z = 16.5$.[35]

2.1 *Technical Advancements*

The MWA has been undergoing various upgrades and transformations throughout its history. Phase I of the MWA,[50] from 2013 to 2017, consisted of 128 beamformed elements arrayed in a semirandom layout with a dense core to allow for high-fidelity imaging and large-scale sensitivity. Phase II of the MWA,[51] from 2017 to 2022, has two configurations depending on the observing program: one imaging layout with longer baselines and one redundant layout with a subset of shorter, random baselines (see Fig. 3), each with 128 beamformed elements. The addition of redundancy has allowed for extensive testing of redundant-based analysis techniques in direct comparison with standard imaging techniques,[52–54] especially in preparation for the next scheduled upgrade.

Phase III of the MWA will be an extensive upgrade of both digital and analog systems, including new beamformers, cables, receivers, and correlator. In the context of EoR, the upgrades to the digital and analogue systems are being driven by the difficulties in calibration. Removing the instrumental signal from the data itself needs to be done at extremely high precision and accuracy, at least one part in 10^5 for both sky-based[20] and redundant-based[55] calibration schemes. Given this requirement, studies on the stability of the beam have begun in earnest to characterize the effects of instrument degradation[29] or deviation[56] on the EoR signal.

These upgrades affect almost every stage of the measurement process, from the element to the correlator. First, the coaxial cables from each antenna to the beamformer box will need to be replaced. Over the course of a decade, the coaxial shielding has degraded in the harsh environment of the Outback, resulting in a sensitivity loss. Next, the receivers will be completely replaced, including the digital system and the analog signal conditioning (ASC) system. An oversampled polyphase filterbank will be used to eliminate loss and spectral artifacts caused by coarse channelization, and when included with increased bit depth for a larger linear-response regime, the EoR spectral requirement of one part in 10^5 can be reached. Improvements to the ASC will also allow the MWA to measure down to 50 MHz, making it a more effective CD experiment. Finally, the MWAX correlator will be able to correlate at least 256 tiles, thus combining the two observing styles using the oversampled coarse channel inputs.

2.2 *Analysis Advancements*

Integrating petabytes of data to reach EoR-levels of sensitivity is compounded in difficulty by the necessary precision and accuracy of the analysis. Various studies have been done within the context of the MWA to understand and reduce systematics, or analysis-based errors, in preparation for the future SKA. These can be grouped into two broad categories: foreground mitigation and precision analysis.

RFI, particularly FM/AM radio and digital TV, is an unwanted foreground and thus must be removed from the data. Even though the MWA is located on a designated radio-quiet site with low RFI background,[40] unchecked faint RFI can still contaminate the EoR signal.[42] This is evident in a recent upper limit on the EoR power spectrum from the MWA, where mitigating ultrafaint digital TV[57] resulted in a factor of 3 improvement.[47]

The refractive effects of the ionosphere can translate into contamination on the EoR signal and thus must be mitigated as well. Using the severity of the positional offsets of point-source foregrounds as a metric for activity,[33] we can now determine the error budget of unmitigated ionospheric effects on EoR analyses.[34,58] These techniques have been used in recent EoR power spectrum upper limits from the MWA to reduce ionospheric systematics[25] and become vitally important for higher redshift measurements[35] due to the wavelength dependence of the ionospheric offsets.

While foreground avoidance techniques do not inherently require subtraction due to the modes of interest, they stand to benefit from an improvement in dynamic range. Thus, even though the MWA probes EoR-window modes, much effort has gone into the characterization of foregrounds, recently via diffuse mapping[59] and with wavelet decomposition of complicated source morphologies.[60]

One of the most dramatic improvements in MWA EoR analysis has been through extreme precision and accuracy, specifically through enforcing spectral smoothness throughout all

software modules. Calibration in particular has been a main focus for the MWA, both in discovering spectral requirements[20,55] and investigating/inventing various calibration styles.[53,54,61] Recently, enforcing spectral smoothness via the instrumental Fourier kernel function through a Tapered Gridded Estimator[62] and with extreme overresolution[63] resulted in significant improvements in MWA upper limits.[25,47,64] Given the importance of spectral smoothness to the power spectrum measurement, current efforts focus on effects of degradation on the instrumental beam[29] and how that propagates to the power spectrum.

To explore observing methodologies and their corresponding analysis techniques, the MWA can observe a singular field (such as LOFAR) or allow the sky to pass overhead (such as HERA). Most published limits with the MWA data come from single-field observations, but investigations into how these results compare to a drift-scan observing programs have shown promising results. First attempted in 2016,[65] these analyses are now comparable with previously published limits,[66] showing significant improvement in precision techniques for various analysis methodologies with the MWA.

2.3 *Limits and Future Developments*

The MWA has a crucial role in SKA development as a pathfinder for the low-frequency program. Indeed, much of the future development of the MWA, including technical and software advancements, is in preparation for the SKA.

Besides the Phase III upgrade already underway, an SKA-MWA signal bridge for cross-correlation is being developed. This will be essential to the EoR experiment due to the harsh spectral requirements on response and calibration. By being able to correlate MWA elements with the SKA prototypes, we can have a stronger view on the future performance of these prototypes and thus be able to change undesired responses prior to the full build. This does come with challenges; the sample rate is unmatched between the MWA and the prototypes, thus a resampling and rate conversion signal bridge will need to be developed alongside Phase III specifications.

Teams around the world are also focusing on analysis software as we approach the SKA-era. Pipelines with various degrees of complexity are being developed, allowing for simultaneous comparisons and cross-pipeline outputs.[67] More complex pipelines will handle the scaling and data load that the SKA will bring (e.g., Ref. 68) while simpler pipelines are the sandbox of scientific testing (e.g., Ref. 61). As these pipelines are improved, the MWA collaboration publishes upper limits using our current data stores to document our progress.

In 2019, a reanalysis of 21 h of Phase I MWA data resulted in a power decrease of almost a factor of 10,[47] owing to careful removal of ultrafaint RFI and improved precision analysis techniques. This was surpassed by an analysis of Phase II MWA data using 40 h of data, which combined both redundant and sky-based analysis techniques to further reduce systematics.[60] In 2020, the best-selected 110 h of MWA data resulted in an upper limit of $\Delta^2_{21} < (43)^2$ mK^2 at $k = 0.14\ h\,\mathrm{Mpc}^{-1}$ and $z = 6.5$,[25] which is to-date the best limit from the MWA. However, a variety of redshifts have been probed by various works with the MWA, including CD redshifts,[35,69] as shown in Fig. 2.

3 Low Frequency Array

3.1 *Project Overview*

LOFAR[15,70] is a radio telescope with its core in the Netherlands and several "international stations" located in multiple European countries. It consists of two distinct aperture arrays: the low-band antenna (LBA) system (30 to 90 MHz) and the high-band antenna (HBA) system (110 to 190 MHz). The observation of the 21-cm signal from the EoR has been one of the drivers behind the design of the telescope: the combination of a dense core array, providing great sensitivity at large spatial scale, and long to very long baselines, allowing for very high-resolution and deep imaging, make it an ideal instrument for precision foreground characterization and subtraction for detection of the cosmological signal.

The LOFAR-EoR Key Science Project mainly targets two deeps fields: the North Celestial Pole (NCP) and the field surrounding the bright compact radio source 3C 196 (see Fig. 3). Currently ≈2480 h of data have been observed with the HBA system. So far, the deepest upper limits of the instrument have been observed with the NCP field. The team published in 2017[71] its first upper limit at $z = 8.3, 9.1$, and 10.1 from one night of observation, and in 2020,[48] an improved upper limit at $z = 9.1$ combining 141 h of data. Step by step, progress has been made, but the experiment remains very challenging. Many studies were needed, and still are, to control the many complex aspects in the signal processing chain in order to be able to reach the expected 21 cm signal strengths that lie two to three orders of magnitude below current upper-limits. Contaminants have many sources: gain-calibration errors due to an incomplete or incorrect sky model,[72] errors in band-pass calibration, beam modeling, residual RFI,[63] as well as chromatic errors introduced due to leakage from the polarized sky into Stokes I[73,74] or due to the ionosphere.[75] These challenges can be met for a large part by a constant improvement of the processing pipeline.

The LOFAR-EoR data processing pipeline consists, in essence, of (1) preprocessing and RFI excision, (2) direction-independent calibration (DI-calibration), (3) direction-dependent calibration (DD-calibration) including subtraction of the sky-model, (4) imaging, (5) residual foreground modelling and removal, and (6) power spectra estimation. All data processing is performed on a dedicated compute-cluster called Dawn,[76] which consists of 48×32 hyper-threaded compute cores and 124 Nvidia K40 GPUs.

3.2 *Analysis Advancements*

The latest LOFAR published upper limit[48] was achieved by making substantial progress in mainly two areas of the processing pipeline: DD-calibration and residual foreground suppression.

LOFAR has a wide field-of-view (about 10 deg between primary beam nulls at 140 MHz) and is susceptible to many DD effects (mainly primary beam and ionospheric effects). Appropriate gain solutions in the source directions are needed to subtract them. Solving in the direction of each and every sources of the sky model would be impractical. Sagecal-CO[77] is used to solve gain solutions simultaneously in 122 clusters of the NCP sky model (which consists of 28,755 components), but additional constraints need to be set to make the problem tractable. To further reduce the number of degrees of freedom, spectral smoothness of the instrumental gains is imposed through strong regularization, which has the combined advantage of reducing calibration noise and making the calibration more resistant to signal loss.[78]

The second area where substantial progress has been made is in the residual foreground suppression strategy. The LOFAR-EoR project relies heavily on the foreground removal paradigm to access the largest available scales of the power-spectra, for which LOFAR is most sensitive. Since the inception of the project, the team has developed and tested several methods to model and subtract foreground emissions: polynomial fitting,[79] Wp smoothing,[80] FastICA, and GMCA.[9] Most of these methods exploit the distinctive spectral correlation signature of the various constituents of the observed signal. While these methods have performed very well on simulated data, their application to real observations has proved more difficult.[81] A new foreground removal algorithm based on Gaussian process regression[82] is now used, which tries to overcome some of the shortfalls found in earlier techniques. In this method, a statistical model of all the components contributing to the observed signal is built using parametric covariance functions. This formulation ensures a relatively unbiased separation of their contribution and an accurate estimation of the uncertainty.

Combining in total 140 h of observation on the NCP at $z = 9$, an upper limit on the 21-cm power spectrum of $\Delta^2_{21} < (72.86)^2$ mK^2 at $k = 0.075\text{h}\,\text{cMpc}^{-1}$ was obtained. This has resulted in a reduction by a factor 10 from our previous upper limit at this redshift.[71] This is the deepest upper limit at $z = 9$, but is not yet optimal as it is affected by a large excess of power, particularly at large scales where the observed residual power is an order of magnitude brighter than the thermal noise power. Nevertheless, this is still an astrophysically interesting upper limit and has been used in several publications to set constraints on the physics of the EoR and on the level of excess radio background (see Sec. 5).

3.3 *Current and Future Developments*

Reaching deeper upper limit requires tackling the issue of excess power. Being partially correlated between observing nights, this excess prevents the residual power from being reduced when they are combined. In particular, taking the diffractive scale as a metric for ionospheric behavior,[75] no clear correlation was found between the excess power and ionospheric activity. This challenges the idea that the ionosphere is a severe and limiting factor, although it might still be an issue at lower noise levels. On the other hand, by dividing the observations into 3-h local sidereal time (LST) bins, it was found that the level of excess was very different from one LST bin to another, and that it was correlated with the flux of bright and distant sources. This suggests that the excess is sky-related, which could be directly (through beam side-lobes) or indirectly (e.g., through gain errors). As a result, several improvements at different stages of the processing pipeline have been planned. In particular, efforts are focused on the calibration steps, but also on the elimination of faint and broadband radio interference, as well as on the suppression of residual foregrounds.

In detail, to reduce calibration noise to a minimum and prevent gain solutions from absorbing flux from sources not part of our sky model, DI-calibration is split into two, with a first step in which spectral-smoothness of the calibration gains is fully enforced and a second step that captures the fast frequency varying but time stable band-pass response of the instrument. While the improvement in the resulting power-spectra is only marginal, this step is now much more resilient to signal loss.[78]

For the DD-calibration step, spectral-smoothness of the calibration gains is also being fully enforced now, and the sky model is being gradually improved with a focus on the brightest sources in the sky (Cassiopea A and Cygnus A) and on the sources located in the second side-lobe of the LOFAR primary beam. The resulting reduction in residual power is substantial, reaching a factor 10 in some parts of the transverse versus line-of-sight power-spectra.

RFI is also a major concern in 21 cm experiments, and in particular faint and broadband RFI which are tricky to detect and filter. The technique of near-field imaging[83] is used to locate local sources of RFI and affected baselines are then flagged accordingly. An additional AOflagger[39] step after DD-calibration is also added. Significant improvements are noted in the cylindrically averaged power-spectra along the horizon line and at low $k_\perp$ (small baselines).

Finally, the residual foreground removal algorithm is being revised to more optimally separate the 21-cm signal from the foregrounds and to make it more robust against signal loss. The parametrized covariance model for both the 21-cm signal and foregrounds is enhanced by incorporating information from simulations via machine learning. The covariance description is also extended to the spatial domain. This is still work in progress but tests on simulation have already shown very promising results.

Despite the challenge of the experiment, the LOFAR-EoR project has made progress toward a detection of the 21 cm from the EoR in recent years and is currently preparing a new multi-redshift upper limit combining the many improvements introduced in the processing pipeline. The LOFAR 2.0 project is also underway. The first stage of upgrades will significantly increase the sensitivity of the LBA system, opening a new window of opportunity to explore the CD with LOFAR, in addition to the ACE project[84] already in operation and uses the AARTFAAC system of LOFAR.

4 Hydrogen Epoch of Reionization Array

4.1 *System Overview*

HERA[85] is a purpose-built radio interferometer for 21-cm intensity mapping of the EoR and CD. It is based in the South African Karoo Astronomy Reserve,[16] and when completed will consist of 350 dish antennas (320 in a dense core with 30 outrigger antennas) packed in a highly redundant and compact hexagonal configuration observing from 50 to 225 MHz. Figure 3 shows a satellite view of the array as of early 2021 (blue-border inset), showing the completed dish deployment of the HERA core.

Relative to configurations like the MWA and LOFAR, which are at least partially optimized for point source imaging, HERA's redundant and compact configuration make it less suitable for high angular resolution imaging, often needed for precise foreground characterization. Instead, HERA's configuration maximizes its sensitivity to the 21-cm power spectrum and allows it to exploit its high degree of baseline redundancy for alternative calibration techniques such as redundant calibration.[16,86,87] This difference in array configuration highlights the stark contrast in how various experiments aim to deal with the foreground contamination problem: either through modeling and subtraction or through avoidance. Indeed, central to HERA's design is the idea of foreground containment and avoidance. A drift-scan array, HERA does not have any moving parts involved with observations, meaning its front-end response is generally quite stable over time. Furthermore, its compact array configuration keeps intrinsic foreground contamination to largely smooth spectral modes, thus preserving more modes for measuring the cosmological signal.[12] Challenges to the foreground avoidance strategy HERA is pursuing include high dynamic range calibration of the antenna response and the mitigation of low-level instrumental systematics such as mutual coupling and cross-talk.

HERA's construction has progressed in two phases. Phase I utilized the existing on-site infrastructure from HERA's predecessor, the Precision Array for Probing the Epoch of Reionization (PAPER) experiment,[88] such as its dipole feeds and signal chains, and combined them with new HERA dishes, which significantly increased HERA's total collecting area compared with PAPER. During Phase I construction of the core of the array (from 2017 to 2018), observations were conducted at night for commissioning and data analysis purposes. A subset of this data forms the basis of HERA's first limit on the 21-cm power spectrum.[89] More recently, HERA construction has progressed to Phase II, which notably involves the installation of new wideband feeds,[90] in addition to the replacement of the front-end signal chain and an upgrade to the correlator.[16] To-date, all of the 330 antennas in the core have been constructed (Fig. 3), with roughly half of them having the new feed and signal chains installed. Current on-site work is focused on installing the remaining feeds and commissioning the system, with full science observations projected for 2022.

4.2 *Advances in Instrument Modeling*

Recent advances in modeling the response of the HERA antenna, feed, and signal chain have come from detailed electromagnetic simulations,[26,90] which include models for the direction-dependent and direction-independent response of both isolated HERA antennas and antennas embedded in a compact array. The predicted beam models are at least partly confirmed by *in-situ* beam modeling derived from imaging drift-scan point source tracks,[28] which shows that the beam is well matched by observations out to the first sidelobe. Current and ongoing work is focused on improving existing models of the far sidelobes and understanding their impact on the 21-cm power spectrum (e.g., Ref. 91).

The embedded-element simulations of Ref. 26 also predict the presence of antenna-to-antenna coupling in the HERA system that may be more complex than originally considered. Indeed, analyses of Phase I data reveal the presence of baseline-based (rather than antenna-based) instrumental coupling systematics.[38,92] While such systematics make detection of the 21-cm signal more difficult, they can be at least partially mitigated. For example, simulated and empirical modeling of the HERA Phase I system by Refs. 38 and 93 shows that antenna-based models for cable reflections and baseline-based, time-domain Fourier filters for antenna coupling can mitigate the observed instrumental systematics by at least two orders of magnitude in the power spectrum.

A deeper understanding of HERA's instrumental response has also come from the development of HERA's calibration pipeline. The 21-cm foreground challenge necessitates that spurious frequency and time structure in the antenna gain solutions be minimized to ensure a clean separation of the cosmological signal. For HERA, the dominant effects are thought to be imperfect models of the sky at the fields used for calibration, as well as deviation from ideal redundancy between nominally redundant baselines. Studies of HERA Phase I data show evidence for such spurious structures, which have yielded insights into the performance of the system, such as the impact of poorly modeled diffuse foreground emission,[36] and the nominal redundancy of HERA

baselines.[87] Such effects will hinder recovery of the 21-cm power spectrum; however, studies indicate they can be at least partially mitigated by smoothing the calibration solutions across time and frequency with tailored Fourier-domain filters.[36,87]

4.3 *Improved Power Spectrum Limits at $z = 7.9$*

Recently, a full analysis of an 18-day dataset from HERA Phase I was completed (∼30 h of integration), yielding new upper limits on the 21-cm EoR power spectrum at $z = 10.4$ and 7.9.[89] These limits are $\Delta^2_{21} \leq (30.76)^2$ mK^2 at $k = 0.192\ h\,\mathrm{Mpc}^{-1}$ and $z = 7.9$ and $\Delta^2_{21} \leq (95.74)^2$ mK^2 at $k = 0.256\ h\,\mathrm{Mpc}^{-1}$ and $z = 10.4$ at 95% confidence.[89] These limits are compared against existing limits in Fig. 1, showing how the $z = 7.9$ limit by HERA improves upon existing limits by over an order of magnitude. The deepest limits achieved a dynamic range of 10^9 with respect to the peak measured foreground power, which was enabled by HERA's emphasis on a smooth instrumental response and a careful accounting of spectral leakage in their analysis pipeline. Furthermore, contrary to other recent limits from competing experiments, HERA's deepest upper limits exhibit rough consistency with thermal noise fluctuations for $k \geq 0.2\ h\,\mathrm{Mpc}^{-1}$, suggesting that the limits could be further improved with more data. This conclusion was derived from a number of statistical null tests that carefully compared the data against HERA's noise models, testing analysis choices such as the frequency window weighting function and the selection of observing nights integrated in the final dataset.[89]

The results presented in Ref. 89 also benefited from a detailed quantification of the uncertainty on the measured power spectrum. Reference 94 provided an overview of the different error-bar methodologies explored by HERA, examining the strengths and weaknesses of various analytic and empirical methods. The chosen methodology for reporting upper limits in Ref. 89 is able to both robustly estimate the thermal noise floor of the data and can also account for boosted noise fluctuations sourced by residual systematic cross terms.

To further bolster confidence in the power spectrum limits set by Ref. 89, an independent validation effort was undertaken to ensure that the HERA Phase I analysis pipeline could recover a known input signal from a realistically corrupted mock HERA data simulation.[95] This effort sought to validate many facets of the analysis pipeline, including the accurate simulation of wide-field foreground and EoR signals, the unbiased recovery of DI gains, the mitigation of baseline-based systematics, and the unbiased estimation of the 21-cm power spectrum. Notably, it tested these components both as individual blocks isolated from other parts of the pipeline and as an end-to-end chain where the pipeline is run on the simulated "raw" data all the way to power spectrum estimation. One of the more tangible outcomes of the validation analysis was the discovery of an ∼7% overall bias in the flux scale of the HERA calibration pipeline, which was then corrected. While the validation effort of Ref. 95 was ambitious in terms of the number of pipeline components tested, it also laid the framework for increasingly more comprehensive validation efforts that will be applied to future HERA results.

Some of the current challenges for HERA data analysis include modeling and mitigating the impact of poorly understood diffuse foregrounds,[22,96] mitigating residual antenna-based and baseline-based instrumental systematics, and identifying weak levels of RFI in the data.[41,57] Examples of recent and ongoing work focused on meeting these challenges include the design of more sophisticated models of instrumental coupling systematics and the constructing visibility filters that remove such systematics to higher dynamic range (e.g., Ref. 97). Current analysis efforts are focused on applying the HERA calibration and power spectrum estimation pipeline on additional Phase I data to achieve possibly deeper limits across $6 < z < 11$, as well as applying it to more recent HERA Phase II data to improve existing power spectrum limits at $z > 12$.

5 Theoretical Modeling

The primary goal for the theoretical modeling of the 21-cm signal is to be able to infer the underlying physics driving the EoR and CD as revealed by the observations. For example, we want to be able to extract information about the nature of these first galaxies (e.g., escape fraction of ionizing radiation). To infer this information, we require three major steps: (i) the ability to characterize the observational data (e.g., with a summary statistic), (ii) a theoretical

model for the 21-cm signal, and (iii) a probabilistic framework from which to infer astrophysical properties using (i) and (ii).

5.1 *Characterizing the 21-cm Signal*

The 21-cm signal observed by radio interferometers varies both spatially (transverse to the observers' line-of-sight) and in frequency (along the observers' line-of-sight). Thus, measuring the 21-cm signal yields a three-dimensional (3D) movie that reveals the timeline of the universe and contains a wealth of both astrophysical and cosmological information.

The sheer volume of data expected is so vast that we cannot conceivably utilize each independent piece of information. Instead, we must reduce the data into a more manageable data-set, typically achieved by statistically averaging the signal using some metric or summary statistic. For studying the EoR, the most commonly adopted and heavily studied statistic in the literature has been the 21-cm power spectrum.[98–101] This is primarily because interferometers natively observe in Fourier space and that the first pathfinders likely can only achieve a low signal-to-noise detection. However, the 21-cm signal is highly non-Gaussian owing to the complex 3D ionization morphology arising from the overlap of distinct ionized regions. Thus, the 21-cm power spectrum is not an optimal statistic to describe the EoR as it crucially misses the non-Gaussian information.

Recently, with the expected order of magnitude increase in sensitivity achievable with the forthcoming SKA, considerable effort has been spent exploring more optimal 21 cm statistics with a specific focus on accessing the non-Gaussian information. The most prominent of these has been the 21-cm bispectrum (e.g., Refs. 102–106): the natural extension of the 21-cm power spectrum, which can notably improve our ability to infer astrophysical information. Alternatively, non-Gaussian information can further be extracted using the Morlet transform[107] along with the higher order moments of the 21-cm brightness temperature PDFs (e.g., Refs. 108 and 109). Further, with the expected imaging capabilities of the SKA, it has also been shown that astrophysical information can equally be extracted from two-dimensional tomographic images of the 21-cm signal. Information can be gleaned about individual ionized bubbles or regions of interest using matched filters[11,110] or convolutional neural networks,[111] the distribution of ionized regions using sophisticated image analysis techniques[112,113] or machine learning,[114] the average properties of galaxies from stacking low-resolution images of the 21-cm signal centered on ionized regions,[115] and the topological and morphological classifications of the 21-cm signal (e.g., Refs. 116–119). Clearly, each approach has its own strengths and weaknesses, and its performance is strongly tied to the specific astrophysical information or feature that is being investigated. It is worth noting that these are only a select few examples of the broach range of approaches being explored in the literature.

5.2 *Modeling the 21-cm Signal*

As the EoR and CD are a complex 3D radiative transfer problem, modeling the 21-cm signal requires numerical simulations. However, current simulations do not have the dynamic range to self-consistently model the EoR (i.e., simultaneously resolve individual stars while tracking large-scale ionization fronts). Instead, in our theoretical toolkit, we have a suite of simulation techniques tailored to exploring specific physical questions trading physical accuracy for computational efficiency. These include coupled hydrodynamical and radiative transfer simulations ($\sim$1 to 10 Mpc's in size), which are extremely computationally intensive that primarily focus on self-consistently exploring first galaxy formation and resultant internal feedback mechanisms (e.g., Refs. 120–122) and more recently (e.g. Refs. 123–125). We also have hydrodynamical or N-body simulations with radiative transfer applied in postprocessing (typically $\sim$10 s 100 Mpc's in size), which are capable of capturing the moderate to large-scale distribution of galaxies responsible for reionization (e.g., Refs. 126–128). Next we have galaxy semianalytic models coupled with seminumerical simulations ($\sim$100 Mpc's in size) which focus on galaxy formation and evolution physics and how these processes imprint their signature on the large-scale 21-cm signal.[129,130] Finally, approximate but computationally efficient seminumerical simulations[131–134] are used for rapid astrophysical parameter space exploration or generating extremely large cosmological volumes (e.g., $\gtrsim$1 Gpc).

5.3 *Inference of Astrophysical Information*

The inference of astrophysical information on the EoR arises from our ability to compare our models of the 21-cm signal to the observational data (through some metric or summary statistic as described above). Here, we want to quantify the likelihood that our theoretical models (given a set of input astrophysical parameters describing the physics) match the observation of the 21-cm signal. Ideally, one would perform this in a fully Bayesian framework; however, this is only currently feasible with seminumerical simulations (i.e., to be able to rapidly explore the vast astrophysical parameter space).

In recent years, several tools have been developed specifically to perform Bayesian inference of the astrophysical parameters describing the EoR. These include (i) flexible, direct approaches that simulate the full 3D signal on-the-fly within the MCMC framework[99] and (ii) emulators[135–139] or deep learning approaches (artificial or convolutional neural networks, e.g., Refs. 140–142) that are specifically trained on a large data-set of simulations to be able to rapidly explore a specific feature or summary statistic (i.e., 21-cm power spectrum) of the observed 21-cm signal. These latter methods can in principle enable the more physically accurate but computationally expensive simulations to be explored in a Bayesian context.

The new upper-limits on the 21-cm signal from the SKA pathfinders have reached the point where they are astrophysically interesting. That is, extreme models of the EoR and CD can begin to be disfavored while also tangibly highlighting the technological advances that have made with the SKA pathfinders. Using some of the inference frameworks described above, we have explored the physical conditions of the IGM, the properties of the high-z galaxies, and information about the excess radio background from LOFAR,[137,139,143] the MWA,[144,145] and HERA.[146] They disfavor: (i) cold reionization scenarios driven by low x-ray luminosities of the first galaxies (i.e., whereby the IGM undergoes no heating) with lower limits placed on the IGM spin temperature and (ii) extreme radio backgrounds that have been proposed to explain the unexpectedly deep EDGES absorption feature.

6 Conclusion

The future SKA telescope will offer a view of the EoR and CD, constraining the processes by which the first stars and galaxies were born and ionized the IGM. Currently, SKA-low pathfinder experiments are hard at work understanding optimal instrument designs and analysis techniques for measuring the 21-cm signal and mitigating the dominant systematic effects associated with low-frequency intensity mapping. These pathfinder experiments, the MWA, LOFAR, and HERA, have complementarities that allow for a robust and wide-ranging effort to make a first detection of the signal, and in doing so demonstrate viability of SKA 21 cm science. In particular, they observe both overlapping and distinct parts of the sky (Fig. 2), which can allow for external cross-check measurements of the same field, as well as an understanding of the benefits of other fields where foregrounds may be better behaved. They also face similar systematic challenges in the shared burden of modeling the foreground and instrumental response to extremely high precision: often studies done with one instrument may reveal particular systematics that are more difficult to understand with another instrument. For example, the MWA GLEAM point source catalog[147] is a key component of HERA's absolute calibration pipeline, which would have otherwise faced more difficulties in modeling point source foregrounds to such precision.

Shared challenges have allowed for the adoption of analysis algorithms between experiments. For example, RFI mitigation software developed for LOFAR[39] is also used on the MWA, and the same ultrafaint RFI mitigation software[57] is used by the MWA and HERA. In addition, redundant calibration techniques have been successfully applied to both HERA and the MWA,[53,87] and statistical foreground modeling software has shown promise on both LOFAR and HERA data.[48,148]

At the same time, these experiments have key differences in their design that make them uniquely situated for specific analyses. LOFAR, for example, is optimized for high dynamic range imaging, DD calibration, and point source characterization, which allows it to make precise foreground models needed for its foreground subtraction approach. HERA, on the other hand, is optimized for maximum sensitivity to a visibility-based 21-cm power spectrum

estimator, has a temporally stable instrument response and leverages its high degree of redundancy for calibration. The MWA strikes a balance between the two with a partial random and redundant layout and is able to implement both image-based and redundancy-based analyses.

Going forward, the analysis work being done between the pathfinders will promote SKA-era science by answering a few key questions, including how can foregrounds be best modeled, subtracted, or mitigated to enable a 21-cm measurement? To what precision does the instrumental response need to be understood and how can this be achieved in real-time for large-antenna arrays? What are the limiting factors in an image-based and a redundancy-based analysis?

Recent developments on these fronts by SKA pathfinders have yielded improved upper limits on the 21-cm power spectrum at the EoR and CD (Fig. 2). Interpretation of these limits require detailed modeling of the 21-cm signal, which also face a host of numerical challenges (sec: theory). Nonetheless, these models show that the recent 21-cm limits are beginning to disfavor extreme astrophysical scenarios of the EoR and CD. Going forward, alternative techniques leveraging higher order statistics and machine learning capabilities are being devised to extract more information from 21 cm measurements.

While key challenges remain in producing a first, robust 21 cm measurement, the combined efforts of the SKA pathfinder experiments are exploring a multitude of analysis approaches that are in many ways highly complementary. These efforts, in addition to the efforts of the wider EoR and CD 21 cm communities, have in turn made significant progress in recent years in understanding how to enable the transformative science of 21-cm intensity mapping in the SKA era.

Acknowledgments

The authors would like to acknowledge the organizers of the 2021 SKA Precursor Conference, where this work was originally shared. GB acknowledges support from the Ministero degli Affari Esteri della Cooperazione Internazionale - Direzione Generale per la Promozione del Sistema Paese Progetto di Grande Rilevanza ZA18GR02. Parts of this research were supported by the Australian Research Council Centre of Excellence for All Sky Astrophysics in 3 Dimensions (ASTRO 3D), through Project No. CE170100013. NK gratefully acknowledges support from the MIT Pappalardo fellowship.

References

1. B. Ciardi and A. Ferrara, "The first cosmic structures and their effects," *Space Sci. Rev.* **116**, 625–705 (2005).
2. S. R. Furlanetto, S. P. Oh, and F. H. Briggs, "Cosmology at low frequencies: the 21 cm transition and the high-redshift Universe," *Phys. Rep.* **433**, 181–301 (2006).
3. M. F. Morales and J. S. B. Wyithe, "Reionization and cosmology with 21-cm fluctuations," *Ann. Rev. Astron. Astrophys.* **48**, 127–171 (2010).
4. J. R. Pritchard and A. Loeb, "21 cm cosmology in the 21st century," *Rep. Prog. Phys.* **75**, 086901 (2012).
5. A. Liu and J. R. Shaw, "Data analysis for precision 21 cm cosmology," *Publ. Astron. Soc. Pac.* **132**, 062001 (2020).
6. M. F. Morales, J. D. Bowman, and J. N. Hewitt, "Improving foreground subtraction in statistical observations of 21 cm emission from the epoch of reionization," *Astrophys. J.* **648**, 767–773 (2006).
7. J. D. Bowman, M. F. Morales, and J. N. Hewitt, "Foreground contamination in interferometric measurements of the redshifted 21 cm power spectrum," *Astrophys. J.* **695**, 183–199 (2009).
8. G. Bernardi et al., "Foregrounds for observations of the cosmological 21 cm line. II. Westerbork observations of the fields around 3C 196 and the North Celestial Pole," *Astron. Astrophys.* **522**, A67 (2010).
9. E. Chapman et al., "The scale of the problem: recovering images of reionization with generalized morphological component analysis," *Mon. Not. R. Astron. Soc.* **429**, 165–176 (2013).

10. M. F. Morales and J. Hewitt, "Toward epoch of reionization measurements with wide-field radio observations," *Astrophys. J.* **615**(1), 7 (2004).
11. K. K. Datta et al., "Prospects of observing a quasar H II region during the epoch of reionization with the redshifted 21-cm signal," *Mon. Not. R. Astron. Soc.* **424**, 762–778 (2012).
12. A. R. Parsons et al., "A per-baseline, delay-spectrum technique for accessing the 21 cm cosmic reionization signature," *Astrophys. J.* **756**, 165 (2012).
13. M. F. Morales et al., "Four fundamental foreground power spectrum shapes for 21 cm cosmology observations," *Astrophys. J.* **752**, 137 (2012).
14. J. C. Pober et al., "Opening the 21 cm epoch of reionization window: measurements of foreground isolation with PAPER," *Astrophys. J.* **768**, L36 (2013).
15. M. P. van Haarlem et al., "LOFAR: the low-frequency array," *Astron. Astrophys.* **556**, A2 (2013).
16. D. DeBoer et al., "Hydrogen Epoch of Reionization Array (HERA)," *Publ. Astron. Soc. Pac.* **129**, 45001 (2017).
17. R. Braun et al., "Anticipated performance of the Square Kilometre Array—phase 1 (SKA1)," arXiv:1912.12699 (2019).
18. J. D. Bowman et al., "An absorption profile centred at 78 megahertz in the sky-averaged spectrum," *Nature* **555**, 67–70 (2018).
19. T. L. Grobler et al., "Calibration artefacts in radio interferometry—I. Ghost sources in Westerbork synthesis radio telescope data," *Mon. Not. R. Astron. Soc.* **439**, 4030–4047 (2014).
20. N. Barry et al., "Calibration requirements for detecting the 21 cm epoch of reionization power spectrum and implications for the SKA," *Mon. Not. R. Astron. Soc.* **461**, 3135–3144 (2016).
21. P. Procopio et al., "A high-resolution foreground model for the MWA EoR1 field: model and implications for EoR power spectrum analysis," *Publ. Astron. Soc. Aust.* **34**, e033 (2017).
22. N. Thyagarajan et al., "Effects of antenna beam chromaticity on Redshifted 21 cm power spectrum and implications for Hydrogen Epoch of Reionization Array," *Astrophys. J.* **825**, 9 (2016).
23. R. C. Joseph et al., "Calibration and 21-cm power spectrum estimation in the presence of antenna beam variations," *Mon. Not. R. Astron. Soc.* **492**, 2017–2028 (2020).
24. A. Nasirudin et al., "The impact of realistic foreground and instrument models on 21 cm epoch of reionization experiments," *Astrophys. J.* **893**, 118 (2020).
25. C. M. Trott et al., "Deep multiredshift limits on Epoch of reionization 21 cm power spectra from four seasons of Murchison widefield array observations," *Mon. Not. R. Astron. Soc.* **493**, 4711–4727 (2020).
26. N. Fagnoni et al., "Understanding the HERA Phase I receiver system with simulations and its impact on the detectability of the EoR delay power spectrum," *Mon. Not. R. Astron. Soc.* **500**, 1232–1242 (2021).
27. N. Orosz et al., "Mitigating the effects of antenna-to-antenna variation on redundant-baseline calibration for 21 cm cosmology," *Mon. Not. R. Astron. Soc.* **487**, 537–549 (2019).
28. C. D. Nunhokee et al., "Measuring HERA's primary beam in situ: methodology and first results," *Astrophys. J.* **897**, 5 (2020).
29. A. Chokshi et al., "Dual polarization measurements of MWA beampatterns at 137 MHz," *Mon. Not. R. Astron. Soc.* **502**, 1990–2004 (2021).
30. S. Yatawatta et al., "Initial deep LOFAR observations of epoch of reionization windows. I. The North Celestial Pole," *Astron. Astrophys.* **550**, A136 (2013).
31. R. J. van Weeren et al., "LOFAR facet calibration," *Astrophys. J. Suppl. Ser.* **223**, 2 (2016).
32. H. K. Vedantham and L. V. E. Koopmans, "Scintillation noise power spectrum and its impact on high-redshift 21-cm observations," *Mon. Not. R. Astron. Soc.* **458**, 3099–3117 (2016).
33. C. H. Jordan et al., "Characterization of the ionosphere above the Murchison radio observatory using the Murchison Widefield Array," *Mon. Not. R. Astron. Soc.* **471**, 3974–3987 (2017).

34. C. M. Trott et al., "Assessment of ionospheric activity tolerances for epoch of reionization science with the Murchison Widefield Array," *Astrophys. J.* **867**(1), 15 (2018).
35. S. Yoshiura et al., "A new MWA limit on the 21 cm power spectrum at redshifts ~13–17," *Mon. Not. R. Astron. Soc.* **505**(4), 4775–4790 (2021).
36. N. S. Kern et al., "Absolute calibration strategies for the Hydrogen Epoch of Reionization Array and their impact on the 21 cm power spectrum," *Astrophys. J.* **890**, 122 (2020).
37. H. Zheng et al., "MITEoR: a scalable interferometer for precision 21 cm cosmology," *Mon. Not. R. Astron. Soc.* **445**, 1084–1103 (2014).
38. N. S. Kern et al., "Mitigating internal instrument coupling for 21 cm cosmology. II. A method demonstration with the Hydrogen Epoch of Reionization Array," *Astrophys. J.* **888**, 70 (2020).
39. A. R. Offringa, J. J. van de Gronde, and J. B. T. M. Roerdink, "A morphological algorithm for improving radio-frequency interference detection," *Astron. Astrophys.* **539**, A95 (2012).
40. A. R. Offringa et al., "The low-frequency environment of the Murchison Widefield Array: radio-frequency interference analysis and mitigation," *Publ. Astron. Soc. Aust.* **32**, e008 (2015).
41. J. Kerrigan et al., "Optimizing sparse RFI prediction using deep learning," *Mon. Not. R. Astron. Soc.* **488**, 2605–2615 (2019).
42. M. J. Wilensky et al., "Quantifying excess power from radio frequency interference in Epoch of Reionization measurements," *Mon. Not. R. Astron. Soc.* **498**, 265–275 (2020).
43. A. Mesinger, B. Greig, and E. Sobacchi, "The evolution of 21 cm structure (EOS): public, large-scale simulations of Cosmic Dawn and reionization," *Mon. Not. R. Astron. Soc.* **459**, 2342–2353 (2016).
44. E. de Lera Acedo et al., "SKA LFAA station design report," arXiv:2003.12744 (2020).
45. A. de Oliveira-Costa et al., "A model of diffuse Galactic radio emission from 10 MHz to 100 GHz," *Mon. Not. R. Astron. Soc.* **388**, 247–260 (2008).
46. H. Zheng et al., "An improved model of diffuse galactic radio emission from 10 MHz to 5 THz," *Mon. Not. R. Astron. Soc.* **464**, 3486–3497 (2017).
47. N. Barry et al., "Improving the epoch of reionization power spectrum results from Murchison Widefield Array season 1 observations," *Astrophys. J.* **884**, 1 (2019).
48. F. G. Mertens et al., "Improved upper limits on the 21 cm signal power spectrum of neutral hydrogen at $z \approx 9.1$ from LOFAR," *Mon. Not. R. Astron. Soc.* **493**, 1662–1685 (2020).
49. http://mwatelescope.org.
50. S. J. Tingay et al., "The Murchison Widefield Array: the Square Kilometre Array precursor at low radio frequencies," *Publ. Astron. Soc. Aust.* **30**, e007 (2013).
51. R. B. Wayth et al., "The Phase II Murchison Widefield Array: design overview," *Publ. Astron. Soc. Aust.* **35**, e033 (2018).
52. J. R. Kerrigan et al., "Improved 21 cm," *Astrophys. J.* **864**(2), 131 (2018).
53. W. Li et al., "Comparing redundant and sky-model-based interferometric calibration: a first look with Phase II of the MWA," *Astrophys. J.* **863**(2), 170 (2018).
54. Z. Zhang et al., "The impact of tandem redundant/sky-based calibration in MWA Phase II data analysis," *Publ. Astron. Soc. Aust.* **37**, e033 (2020).
55. R. Byrne et al., "Fundamental limitations on the calibration of redundant 21 cm cosmology instruments and implications for HERA and the SKA," *Astrophys. J.* **875**, 70 (2019).
56. R. C. Joseph, C. M. Trott, and R. B. Wayth, "The bias and uncertainty of redundant and sky-based calibration under realistic sky and telescope conditions," *The Astronomical Journal* **156**, 285 (2018).
57. M. J. Wilensky et al., "Absolving the SSINS of precision interferometric radio data: a new technique for mitigating faint radio frequency interference," *Publ. Astron. Soc. Pac.* **131**, 114507 (2019).
58. J. K. Chege et al., "Simulations of ionospheric refraction on radio interferometric data," *Publ. Astron. Soc. Aust.* **38**, e028 (2021).
59. R. Byrne et al., "A map of diffuse radio emission at 182 MHz to enhance epoch of reionization observations in the southern hemisphere," arXiv:2107.11487 (2021).

60. J. L. B. Line et al., "Modelling and peeling extended sources with shapelets: a Fornax A case study," *Publ. Astron. Soc. Aust.* **37**, e027 (2020).
61. N. Barry et al., "The FHD/εppsilon epoch of reionisation power spectrum pipeline," *Publ. Astron. Soc. Aust.* **36**, e026 (2019).
62. S. Choudhuri et al., "Tapering the sky response for angular power spectrum estimation from low-frequency radio-interferometric data," *Mon. Not. R. Astron. Soc.* **459**, 151–156 (2016).
63. A. R. Offringa, F. Mertens, and L. V. E. Koopmans, "The impact of interference excision on 21-cm epoch of reionization power spectrum analyses," *Mon. Not. R. Astron. Soc.* **484**, 2866–2875 (2019).
64. W. Li et al., "First season MWA Phase II epoch of reionization power spectrum results at redshift 7," *Astrophys. J.* **887**, 141 (2019).
65. S. Paul et al., "Delay spectrum with phase-tracking arrays: extracting the HI power spectrum from the epoch of reionization," *Astrophys. J.* **833**, 213 (2016).
66. A. K. Patwa, S. Sethi, and K. S. Dwarakanath, "Extracting the 21 cm EoR signal using MWA drift scan data," *Mon. Not. R. Astron. Soc.* **504**, 2062–2072 (2021).
67. D. C. Jacobs et al., "The Murchison Widefield Array 21 cm power spectrum analysis methodology," arXiv:1605.06978 astro-ph (2016).
68. D. Mitchell et al., "Real-time calibration of the Murchison Widefield Array," *IEEE J. Sel. Top. Signal Process.* **2**, 707–717 (2008).
69. A. Ewall-Wice et al., "First limits on the 21 cm power spectrum during the Epoch of x-ray heating," *Mon. Not. R. Astron. Soc.* **460**, 4320–4347 (2016).
70. http://www.lofar.org
71. A. H. Patil et al., "Upper limits on the 21 cm epoch of reionization power spectrum from one night with LOFAR," *Astrophys. J.* **838**, 65 (2017).
72. A. H. Patil et al., "Systematic biases in low-frequency radio interferometric data due to calibration: the LOFAR-EoR case," *Mon. Not. R. Astron. Soc.* **463**, 4317–4330 (2016).
73. V. Jelić et al., "Realistic simulations of the Galactic polarized foreground: consequences for 21-cm reionization detection experiments," *Mon. Not. R. Astron. Soc.* **409**, 1647–1659 (2010).
74. K. M. B. Asad et al., "Polarization leakage in epoch of reionization windows - I. Low Frequency Array observations of the 3C196 field," *Mon. Not. R. Astron. Soc.* **451**, 3709–3727 (2015).
75. M. Mevius et al., "Probing ionospheric structures using the LOFAR radio telescope," *Radio Sci.* **51**, 927–941 (2016).
76. V. Pandey et al., "An integrated HPC system for the LOFAR EoR project," in *ADASS XXVIV. ASP Conf. Ser.*, Vol. 524, R. Pizzo et al., Eds. (2020).
77. S. Yatawatta, "Fine tuning consensus optimization for distributed radio interferometric calibration," arXiv:1605.09219 (2016).
78. A. M. Sardarabadi and L. V. E. Koopmans, "Quantifying suppression of the cosmological 21-cm signal due to direction-dependent gain calibration in radio interferometers," *Mon. Not. R. Astron. Soc.* **483**, 5480–5490 (2019).
79. V. Jelić et al., "Foreground simulations for the LOFAR-epoch of reionization experiment," *Mon. Not. R. Astron. Soc.* **389**, 1319–1335 (2008).
80. G. Harker et al., "Non-parametric foreground subtraction for 21-cm epoch of reionization experiments," *Mon. Not. R. Astron. Soc.* **397**, 1138–1152 (2009).
81. I. Hothi et al., "Comparing foreground removal techniques for recovery of the LOFAR-EoR 21 cm power spectrum," *Mon. Not. R. Astron. Soc.* **500**, 2264–2277 (2021).
82. F. G. Mertens, A. Ghosh, and L. V. E. Koopmans, "Statistical 21-cm signal separation via Gaussian process regression analysis," *Mon. Not. R. Astron. Soc.* **478**, 3640–3652 (2018).
83. G. Paciga et al., "The GMRT epoch of reionization experiment: a new upper limit on the neutral hydrogen power spectrum at $z \approx 8.6$," *Mon. Not. R. Astron. Soc.* **413**, 1174–1183 (2011).
84. B. K. Gehlot et al., "The AARTFAAC cosmic explorer: observations of the 21-cm power spectrum in the EDGES absorption trough," *Mon. Not. R. Astron. Soc.* **499**, 4158–4173 (2020).

85. http://reionization.org/.
86. J. Dillon and A. Parsons, "Redundant array configurations for 21 cm cosmology," *Astrophys. J.* **826**, 181 (2016).
87. J. S. Dillon et al., "Redundant-baseline calibration of the Hydrogen Epoch of Reionization Array," *Mon. Not. R. Astron. Soc.* **499**, 5840–5861 (2020).
88. A. R. Parsons et al., "The precision array for probing the epoch of re-ionization: eight station results," *Astron. J.* **139**, 1468–1480 (2010).
89. The HERA Collaborationet al., "First results from HERA Phase I: upper limits on the epoch of reionization 21 cm power spectrum," arXiv:2108.02263 (2021).
90. N. Fagnoni et al., "Design of the new wideband vivaldi feed for the HERA radio-telescope Phase II," arXiv:2009.07939 (2020).
91. S. Choudhuri, P. Bull, and H. Garsden, "Patterns of primary beam non-redundancy in close-packed 21 cm array observations," *Mon. Not. R. Astron. Soc.* **506**, 2066–2088 (2021).
92. N. Thyagarajan et al., "Detection of cosmic structures using the bispectrum phase. II. First results from application to cosmic reionization using the Hydrogen Epoch of Reionization Array," *Phys. Rev. D* **102**, 022002 (2020).
93. N. S. Kern et al., "Mitigating internal instrument coupling for 21 cm cosmology. I. Temporal and spectral modeling in simulations," *Astrophys. J.* **884**, 105 (2019).
94. J. Tan et al., "Methods of error estimation for delay power spectra in 21 cm cosmology," arXiv:2103.09941 (2021).
95. J. E. Aguirre et al., "Validation of the HERA Phase I epoch of reionization 21 cm power spectrum software pipeline," arXiv:2104.09547 (2021).
96. C. L. Carilli et al., "Imaging and modeling data from the Hydrogen Epoch of Reionization Array," *Astrophys. J. Suppl. Ser.* **247**, 67 (2020).
97. A. Ewall-Wice et al., "DAYENU: a simple filter of smooth foregrounds for intensity mapping power spectra," *Mon. Not. R. Astron. Soc.* **500**, 5195–5213 (2021).
98. J. C. Pober et al., "What next-generation 21 cm power spectrum measurements can teach us about the epoch of reionization," *Astrophys. J.* **782**, 66 (2014).
99. B. Greig and A. Mesinger, "21CMMC: an MCMC analysis tool enabling astrophysical parameter studies of the cosmic 21 cm signal," *Mon. Not. R. Astron. Soc.* **449**, 4246–4263 (2015).
100. S. Hassan et al., "Epoch of reionization 21 cm forecasting from MCMC-constrained semi-numerical models," *Mon. Not. R. Astron. Soc.* **468**, 122–139 (2017).
101. A. Cohen, A. Fialkov, and R. Barkana, "Charting the parameter space of the 21-cm power spectrum," *Mon. Not. R. Astron. Soc.* **478**, 2193–2217 (2018).
102. S. Yoshiura et al., "Sensitivity for 21 cm bispectrum from epoch of reionization," *Mon. Not. R. Astron. Soc.* **451**, 266–274 (2015).
103. H. Shimabukuro et al., "Constraining the epoch-of-reionization model parameters with the 21-cm bispectrum," *Mon. Not. R. Astron. Soc.* **468**, 1542–1550 (2017).
104. S. Majumdar et al., "Quantifying the non-Gaussianity in the EoR 21-cm signal through bispectrum," *Mon. Not. R. Astron. Soc.* **476**, 4007–4024 (2018).
105. A. Hutter et al., "The 21 cm bispectrum during reionization: a tracer of the ionization topology," *Mon. Not. R. Astron. Soc.* **492**, 653–667 (2020).
106. C. A. Watkinson et al., "The 21-cm bispectrum as a probe of non-Gaussianities due to x-ray heating," *Mon. Not. R. Astron. Soc.* **482**, 2653–2669 (2019).
107. C. M. Trott, "Exploring the evolution of reionization using a wavelet transform and the light cone effect," *Mon. Not. R. Astron. Soc.* **461**, 126–135 (2016).
108. C. A. Watkinson and J. R. Pritchard, "The impact of spin-temperature fluctuations on the 21-cm moments," *Mon. Not. R. Astron. Soc.* **454**, 1416–1431 (2015).
109. K. Kubota et al., "Expected constraints on models of the epoch of reionization with the variance and skewness in redshifted 21 cm-line fluctuations," *Publ. Astron. Soc. Jpn.* **68**, 61 (2016).
110. S. Majumdar, S. Bharadwaj, and T. R. Choudhury, "Constraining quasar and intergalactic medium properties through bubble detection in redshifted 21-cm maps," *Mon. Not. R. Astron. Soc.* **426**, 3178–3194 (2012).

111. S. Hassan et al., "Identifying reionization sources from 21 cm maps using convolutional neural networks," *Mon. Not. R. Astron. Soc.* **483**, 2524–2537 (2019).
112. K. Kakiichi et al., "Recovering the H II region size statistics from 21-cm tomography," *Mon. Not. R. Astron. Soc.* **471**, 1936–1954 (2017).
113. S. K. Giri, G. Mellema, and R. Ghara, "Optimal identification of H II regions during reionization in 21-cm observations," *Mon. Not. R. Astron. Soc.* **479**, 5596–5611 (2018).
114. M. Bianco et al., "Deep learning approach for identification of H II regions during reionization in 21-cm observations," *Mon. Not. R. Astron. Soc.* **505**, 3982–3997 (2021).
115. J. E. Davies et al., "Stacking redshifted 21 cm images of H II regions around high-redshift galaxies as a probe of early reionization," *Mon. Not. R. Astron. Soc.* **501**, 146–156 (2021).
116. S. Yoshiura et al., "Studying topological structure of 21-cm line fluctuations with 3D Minkowski functionals before reionization," *Mon. Not. R. Astron. Soc.* **465**, 394–402 (2017).
117. A. Kapahtia et al., "A novel probe of ionized bubble shape and size statistics of the epoch of reionization using the contour Minkowski tensor," *J. Cosmol. Astropart. Phys.* **2018**, 011 (2018).
118. W. Elbers and R. van de Weygaert, "Persistent topology of the reionization bubble network—I. Formalism and phenomenology," *Mon. Not. R. Astron. Soc.* **486**, 1523–1538 (2019).
119. S. K. Giri and G. Mellema, "Measuring the topology of reionization with Betti numbers," *Mon. Not. R. Astron. Soc.* **505**, 1863–1877 (2021).
120. J. Rosdahl et al., "The SPHINX cosmological simulations of the first billion years: the impact of binary stars on reionization," *Mon. Not. R. Astron. Soc.* **479**, 994–1016 (2018).
121. X. Wu et al., "Simulating the effect of photoheating feedback during reionization," *Mon. Not. R. Astron. Soc.* **488**, 419–437 (2019).
122. P. Ocvirk et al., "Cosmic Dawn II (CoDa II): a new radiation-hydrodynamics simulation of the self-consistent coupling of galaxy formation and reionization," *Mon. Not. R. Astron. Soc.* **496**, 4087–4107 (2020).
123. R. Kannan et al., "Introducing the THESAN project: radiation-magneto-hydrodynamic simulations of the epoch of reionization," arXiv:2110.00584 (2021).
124. E. Garaldi et al., "The THESAN project: properties of the intergalactic medium and its connection to reionization-era galaxies," arXiv:2110.01628 (2021).
125. A. Smith et al., "The THESAN project: Lyman-alpha emission and transmission during the Epoch of Reionization," arXiv:2110.02966 (2021).
126. K. L. Dixon et al., "The large-scale observational signatures of low-mass galaxies during reionization," *Mon. Not. R. Astron. Soc.* **456**, 3011–3029 (2016).
127. B. Semelin et al., "21SSD: a public data base of simulated 21-cm signals from the epoch of reionization," *Mon. Not. R. Astron. Soc.* **472**, 4508–4520 (2017).
128. M. B. Eide et al., "Large-scale simulations of H and He reionization and heating driven by stars and more energetic sources," *Mon. Not. R. Astron. Soc.* **498**, 6083–6099 (2020).
129. S. J. Mutch et al., "Dark-ages reionization and galaxy formation simulation - III. Modelling galaxy formation and the epoch of reionization," *Mon. Not. R. Astron. Soc.* **462**, 250–276 (2016).
130. A. Hutter et al., "Astraeus I: the interplay between galaxy formation and reionization," *Mon. Not. R. Astron. Soc.* **503**, 3698–3723 (2021).
131. M. G. Santos et al., "Fast large volume simulations of the 21-cm signal from the reionization and pre-reionization epochs," *Mon. Not. R. Astron. Soc.* **406**, 2421–2432 (2010).
132. A. Mesinger, S. Furlanetto, and R. Cen, "21CMFAST: a fast, seminumerical simulation of the high-redshift 21-cm signal," *Mon. Not. R. Astron. Soc.* **411**, 955–972 (2011).
133. A. Fialkov, R. Barkana, and E. Visbal, "The observable signature of late heating of the Universe during cosmic reionization," *Nature* **506**, 197–199 (2014).
134. A. Hutter, "The accuracy of seminumerical reionization models in comparison with radiative transfer simulations," *Mon. Not. R. Astron. Soc.* **477**, 1549–1566 (2018).
135. N. S. Kern et al., "Emulating simulations of Cosmic Dawn for 21 cm power spectrum constraints on cosmology, reionization, and x-ray heating," *Astrophys. J.* **848**, 23 (2017).

136. C. J. Schmit and J. R. Pritchard, "Emulation of reionization simulations for Bayesian inference of astrophysics parameters using neural networks," *Mon. Not. R. Astron. Soc.* **475**, 1213–1223 (2018).
137. R. Mondal et al., "Tight constraints on the excess radio background at $z = 9.1$ from LOFAR," *Mon. Not. R. Astron. Soc.* **498**, 4178–4191 (2020).
138. A. Cohen et al., "Emulating the global 21-cm signal from Cosmic Dawn and reionization," *Mon. Not. R. Astron. Soc.* **495**, 4845–4859 (2020).
139. R. Ghara et al., "Constraining the intergalactic medium at z = 9.1 using LOFAR Epoch of Reionization observations," *Mon. Not. R. Astron. Soc.* **493**, 4728–4747 (2020).
140. H. Shimabukuro and B. Semelin, "Analysing the 21 cm signal from the epoch of reionization with artificial neural networks," *Mon. Not. R. Astron. Soc.* **468**, 3869–3877 (2017).
141. A. Doussot, E. Eames, and B. Semelin, "Improved supervised learning methods for EoR parameters reconstruction," arXiv:1904.04106 (2019).
142. N. Gillet et al., "Deep learning from 21-cm tomography of the Cosmic Dawn and reionization," *Mon. Not. R. Astron. Soc.* **484**, 282–293 (2019).
143. B. Greig et al., "Interpreting LOFAR 21-cm signal upper limits at z = 9.1 in the context of high-z galaxy and reionization observations," *Mon. Not. R. Astron. Soc.* **501**, 1–13 (2021).
144. R. Ghara et al., "Constraining the state of the intergalactic medium during the Epoch of reionization using MWA 21-cm signal observations," *Mon. Not. R. Astron. Soc.* **503**, 4551–4562 (2021).
145. B. Greig et al., "Exploring reionization and high-z galaxy observables with recent multi-redshift MWA upper limits on the 21-cm signal," *Mon. Not. R. Astron. Soc.* **500**, 5322–5335 (2021).
146. The HERA Collaborationet al., "HERA Phase I limits on the cosmic 21-cm signal: constraints on astrophysics and cosmology during the epoch of reionization," arXiv:2108.07282 (2021).
147. N. Hurley-Walker et al., "GaLactic and extragalactic all-sky Murchison Widefield Array (GLEAM) survey—I. A low-frequency extragalactic catalogue," *Mon. Not. R. Astron. Soc.* **464**, 1146–1167 (2016).
148. A. Ghosh et al., "Foreground modelling via Gaussian process regression: an application to HERA data," *Mon. Not. R. Astron. Soc.* **495**, 2813–2826 (2020).

Nichole Barry is a postdoctoral fellow at the University of Melbourne, and an incoming Forrest fellow at Curtin University. She received her PhD from University of Washington in 2018 with a focus on calibration techniques for the MWA.

Gianni Bernardi received his PhD at Bologna University in 2004. He is currently a researcher at INAF–IRA and a visiting professor at Rhodes University. He works on observational 21-cm cosmology.

Bradley Greig is an ASTRO 3D fellow at the University of Melbourne, where he also received his PhD. He focuses on astrophysical parameter inference on the EoR and CD using MCMC techniques.

Nicholas Kern is a Pappalardo postdoctoral fellow in the Department of Physics and the Kavli Institute for Astrophysics and Space Research at MIT. He received his PhD in astrophysics from UC Berkeley in 2020 working on data analysis for 21-cm intensity mapping.

Florent Mertens is a postdoctoral researcher at LERMA, Observatoire de Paris, and received his PhD at the Max Planck Institute in Bonn. His research focuses on observational cosmology, with a particular emphasis on the 21-cm line of neutral hydrogen.